Journal of Materials Chemistry

Cite this: J. Mater. Chem., 2012, 22, 13311

www.rsc.org/materials

PAPER

2D hexagonal mesoporous platinum films exhibiting biaxial, in-plane pore alignment†

Kaleem Abbas Asghar, Joanne Margaret Elliott* and Adam Michael Squires

Received 20th March 2012, Accepted 23rd May 2012
DOI: 10.1039/c2jm31731a

The synthesis of 2D hexagonal mesoporous platinum films with biaxial, in-plane pore alignment is demonstrated by electrodeposition through an aligned lyotropic liquid crystal templating phase. Shear force is used to align a hexagonal lyotropic liquid crystalline templating phase of an inexpensive and a commercially available surfactant, $C_{16}EO_{10}$, at the surface of an electrode. Electrodeposition and subsequent characterisation of the films produced shows that the orientation and alignment of the phase is transferred to the deposited material. Transmission electron microscopy confirms the expected nanostructure of the films, whilst transmission and grazing incidence small angle X-ray scattering analysis confirms biaxial, in plane alignment of the pore structure. In addition further electrochemical studies in dilute sulfuric acid and methanol show that the pores are accessible to electrolyte solution as indicated by a large current flow; the modified electrode therefore has a high surface area, that catalyses methanol oxidation, and the pores have a very large aspect ratio (of theoretical maximum 2×10^5). Films with such aligned mesoporosity will advance the field of nanotechnology where the control of pore structure is paramount. The method reported is sufficiently generic to be used to control the structure and order of many materials, thus increasing the potential for the development of a wide range of novel electronic and optical devices.

Introduction

Lyotropic liquid crystal templating is a versatile and facile way of producing mesoporous materials,[1–5] and reviews of the area are available.[6,7] Preparation techniques include both chemical[3,8] and electrochemical[4,9] methods and a wide variety of materials have been produced including inorganic materials,[10] polymers,[11] semiconductors,[12,13] metal oxides,[14] metals,[3,4,8,9,15–17] hybrid materials[18] and alloys.[19] During the last decade scientists have been interested not only in synthesizing new mesoporous materials but also in trying to control their form and order. Thus whether a material is produced in the form of a film, as rods, as tubes, as particles, or as a monolith has become increasingly important.[20,21] Mesopores proffer a high surface area and this, tailored with the ability to control their structure[22] and accessibility, makes successful application of mesoporous materials in fields such as catalysis,[4,7,23,24] analysis,[25–29] separation technology,[30,31] optical devices[32,33] and biomedical science very likely.[34] Materials with controlled pore alignment will exhibit long range order in addition to local order and the ability to produce films containing aligned pores is thus highly desirable;[35–37] in particular the materials will proffer enhanced separation properties[30,31] and optical properties.[32] However, the ability to fabricate a highly oriented and perfectly aligned mesoporous material represents a significant challenge; there are some interesting reports in the literature associated with mesoporous silica,[38] silica–titania composite[33] and metal oxide films[39] all produced using chemical methods but none for mesoporous metals and none using electrodeposition.

In 1997 Attard demonstrated that metallic mesoporous films (H_1-ePt) could be produced simply by electrodeposition from the desired mesophase[4] and based on STM measurement this paper reported that the mesopores appeared to be "on average, at an angle of 20° with respect to the normal to the plane of the electrode". Many publications have since used the method of lyotropic liquid crystal templating to produce mesoporous films; however the ability to electrodeposit a film with controlled pore orientation has yet to be demonstrated. Here in this paper for the

Department of Chemistry, The University of Reading, Whiteknights, Reading, RG6 6AD, Berkshire, UK. E-mail: j.m.elliott@reading.ac.uk; Fax: +44 (0) 118 378 6331; Tel: +44 (0) 118 378 6342

† Electronic supplementary information (ESI) available: SI1 – SEM images of the large area electrode. SI2 – transmission SAXS data for the multi domain phase. SI3 – a schematic diagram showing sample loading for transmission SAXS analysis. SI4 – transmission SAXS data for a multi domain H_1-ePt film. SI5 and SI6 – data to show the effect of orientation of the ridges of the support electrode upon the resulting electrodeposited films. SI7 – schematic diagram showing sample loading for GI-SAXS analysis when the X-ray beam was parallel to the direction of shear. SI8 – transmission SAXS data for a H_1-ePt film deposited from a shear aligned, heat treated, phase. SI9 – TEM images for a H_1-ePt film. SI10 – schematic diagram showing sample loading for GI-SAXS where the X-ray beam was perpendicular to the direction of shear. SI11 – GI-SAXS analysis of an aligned (H_1-ePt) films where the beam was perpendicular the direction of shear. See DOI: 10.1039/c2jm31731a

first time, we demonstrate that good control of the alignment, orientation and long range order of the mesoporous structure of H_1-ePt films can be achieved by shear alignment[34] of the templating phase at the surface of the electrode prior to electrodeposition. We have for the first time demonstrated the ability to electrodeposit metal films with biaxial pore alignment, where the pores all lie in the plane of the electrode and all point in the same direction.

It should be noted that the approach presented here is entirely novel; first, this work focuses on the formation of a metallic structure with biaxially aligned mesopores, and secondly, it involves the use of electrodeposition to form thin films with aligned mesopores. It is believed, however, that this approach is sufficiently general to be extended to other lyotropic liquid crystal templating systems and other electrodeposited materials and thus should be of widespread interest.

Experimental

The surfactant polyoxyethylene (10) cetyl ether ($C_{16}EO_{10}$), otherwise known as Brij-56, and hexachloroplatinic acid aqueous solution (HCPA, 0.2 M, 99.9%) were purchased from Sigma-Aldrich and were used as received. Pure water prepared by passing deionised, distilled water through a Milli-Q water purification system was used throughout. A binary liquid crystalline phase comprised of 50 wt% of $C_{16}EO_{10}$–H_2O and a pseudobinary liquid crystalline phase comprised of 50 wt% of $C_{16}EO_{10}$–HCPA were prepared by manual mixing in a fashion similar to that reported previously.[40]

Small angle X-ray scattering analysis of the phase behaviour of the liquid crystalline mixtures was performed on a Bruker AXS Nanostar system, fitted with a Vantec 2000 photon counting 2D detector with variable camera length. This machine used a Cu K_α ($\lambda = 1.54$ Å) source at 45 kV and had a compact 3-pinhole collimation system which formed a well-defined spot size (0.4 to 0.8 mm). The mixtures were prepared in a sandwich cell, made of a silicone rubber spacer wrapped in polyimide sticky tape, which was then mounted into a Linkam sample holder. All temperature-controlled measurements were performed on an mri Physikalische Geräte GmbH high-temperature heating stage (mri-0065152/heating stage); the mixtures were heated between 20 and 80 °C at a ramp rate of 3 °C min^{-1}. All 2D scattering patterns were analysed and integrated (both radially and azimuthally) to produce 1D intensity profiles using Image J together with YAX macro suite.[41]

Electrochemical deposition experiments were carried out from the pseudobinary templating phase in a 3-electrode electrochemical cell using either a gold or platinum working electrode (large or small area (0.2–0.4 cm^2 or 2×10^{-3} cm^2) respectively), a platinum counter electrode and a silver/silver chloride (Ag/AgCl) reference electrode (+0.248 V *vs.* NHE).

The large area gold working electrodes were made from archival gold DVD-R discs purchased from Delkin Devices, UK. The 24 carat gold reflective layer (≈80 to 100 nm thick) of the DVD-R discs was used as a substrate for electrodeposition without any prior cleaning. The gold layer was exposed by removing the top polycarbonate coating with the help of tweezers. The resulting gold electrode was examined by scanning electron microscopy and shown to be ridged (see ESI, Fig. SI1a†). The small area platinum working electrode was a 0.5 mm diameter sealed platinum wire, polished and cycled in sulfuric acid prior to use in the standard fashion.[42]

H_1-ePt films were prepared by stepping the potential between +0.5 and −0.1 V *vs.* Ag/AgCl and passing a charge density (Q) of between 0.5 and 0.8 C cm^{-2}. A water bath (Grant Y6) was used to control the temperature. After washing with water the films were characterized using both transmission and grazing incidence SAXS on a Bruker AXS Nanostar system at camera lengths of 67 and 107 cm respectively. Films were mounted on a flat metal grid for transmission X-ray scattering measurements and mounted on a motor controlled rotating sample stage for grazing incidence scattering measurements. Films were also analysed by voltammetric cycling in 0.5 M aqueous sulfuric acid (where roughness factor, R_f, was determined in the standard fashion[42]) and also in a mixture of 0.5 M sulfuric acid and 0.5 M methanol between approximately +1.2 and −0.30 V *vs.* Ag/AgCl at 200 mV s^{-1}.

A Philips CM20 transmission electron microscope, operating at 200 kV, was used to investigate the porosity and the nanostructure of the films. The images were calibrated and analysed using Scandium software. An FEI Quanta FEG 600 Environmental Scanning Electron Microscope was also used to image the surface of the depositing substrates and the mesoporous metal films (see ESI, Fig. SI1b and SI1c†).

Results and discussion

Conventionally a homogenous structure-directing hexagonal templating phase is produced *via* manual mixing and this process is expected to lead to the formation of a poly domain templating phase with short range order. The homogeneous phase will have short range order associated with the packing of the rod-like micelles on a hexagonal lattice of regular geometry but no overall long range order, as the sample will contain hexagonal domains oriented in all directions in 3D space. SAXS data for such a conventionally prepared H_1 phase are shown in Fig. 1. Fig. 1a shows the corresponding 2D SAXS pattern; a clear set of isotropic rings was observed confirming the 3D arrangement of the hexagonal domains. Fig. 1b shows an azimuthal integration scan of the 2D SAXS pattern for the multi domain H_1 phase; as expected little variation in the intensity of the rings was observed (for clarity the azimuthal angle is also shown in Fig. 1a). Fig. 1c shows the corresponding radial integration scan for the H_1 phase collected over a range of temperatures. The H_1 phase was heated from 30 to 80 °C and then cooled back to 30 °C, and SAXS data were collected regularly. At 30 °C three Bragg peaks typical for hexagonal symmetry[43] with relative peak positions of $\sqrt{1}$, $\sqrt{3}$ and $\sqrt{4}$ were observed confirming the expected short range structure. The lattice parameter for this H_1 phase was found to be $a = 76 \pm 1$ Å where $a = (d_{100} \times 2)/\sqrt{3}$ and d_{100} is the d-spacing of the first reflection. The H_1 phase was found to be stable across quite a wide temperature range, however only one broad peak was observed at ≥72 °C, indicating that the mixture had formed an isotropic L_1 phase; this was observed to be stable up to 80 °C (the highest temperature investigated). When this mixture was subsequently cooled it returned to a multi domain H_1 phase. The lattice parameter of the H_1 phase before and after heating was found to be unchanged at 76 ± 1 Å. Representative 2D SAXS patterns for 50, 70, 75 and 80 °C are shown in the ESI (Fig. SI2†).

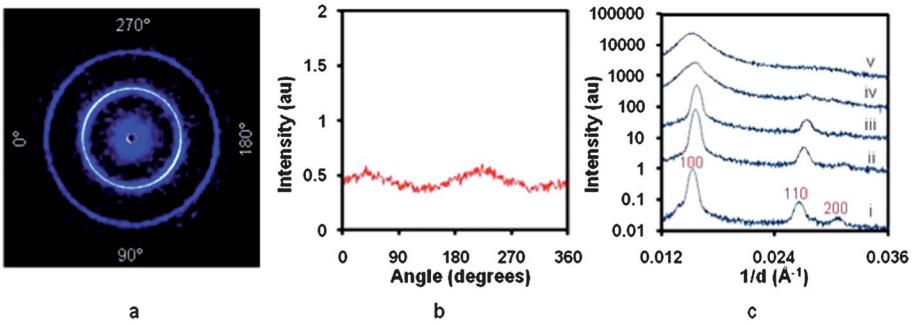

Fig. 1 SAXS analysis of a $C_{16}EO_{10}$–H_2O multi domain hexagonal (H_1) phase; (a) 2D SAXS pattern collected at 30 °C, over 300 s, (b) azimuthally integrated SAXS pattern (inner ring) collected at 30 °C, and (c) radially integrated 1D SAXS patterns collected at (i) 30, (ii) 50, (iii) 70, (iv) 75 and (v) 80 °C.

Electrodeposition was then carried out from such a multi domain hexagonal templating phase. The electrode was first inserted into the electrochemical cell containing an isotropic micellar phase at 80 °C; the electrode was allowed to equilibrate for 5 min before rapidly cooling to 30 °C prior to deposition. After deposition the H_1-ePt film was prepared for SAXS analysis. A schematic diagram showing horizontal sample loading is shown in the ESI (Fig. SI3†). Fig. 2a shows an example of the 2D SAXS pattern obtained; again a clear set of rings was observed. Fig. 2b shows an azimuthal integration scan of the SAXS pattern for the film, no variation in intensity was observed confirming a lack of long range order in the nanostructure of the film. Fig. 2c shows the corresponding radial integration scan; two Bragg peaks typical of hexagonal symmetry with relative peak positions of $\sqrt{1}$:$\sqrt{3}$, were observed confirming the presence of short range order in the nanostructure of the film. The lattice parameter for this film was found to be 75 ± 1 Å which is in good agreement with the templating phase itself. The analysis was repeated on different areas of the electrode (controlled using an x, y stage), similar results were obtained and further examples of the observed 2D SAXS patterns are given in the ESI (Fig. SI4†). Analysis of several films prepared in this fashion produced broadly similar results.

As stated earlier the ability to produce a H_1-ePt film with a long range, uniform, uniaxial or biaxial, hexagonal nanostructure in a single domain instead of a short range, random, poly domain nanostructure is highly desirable, yet challenging. In an effort to face this challenge the effects of shear force upon phase orientation were therefore investigated. In this case the H_1 phase was applied to the surface of an electrode using shear force (the force was applied parallel to the substrate surface in one particular direction, moving from the top of the electrode, T, to the bottom of the electrode, B) as illustrated in Fig. 3. SAXS data for a phase treated in this way, where the direction of shear is loaded horizontally, are shown in Fig. 4. Fig. 4a shows the corresponding 2D SAXS pattern; a clear set of arcs were observed indicating preferred alignment of the H_1 phase, with the cylinders oriented parallel to the shear direction (in plane with the supporting electrode, in contrast to the data presented in Fig. 1a). Fig. 4b shows the corresponding azimuthal integration; as expected two very sharp peaks centered at 92 and 275° were observed, supporting alignment of the H_1 phase planar to the electrode surface. The full width at half-maximum (FWHM) values for the first and the second azimuthal peaks was found to be 19 ± 1 and 20 ± 1° respectively indicating relatively good alignment and long range order in the H_1 phase. The corresponding radial integration scan in Fig. 4c again shows three Bragg peaks typical of hexagonal symmetry with relative peak to peak positions of $\sqrt{1}$, $\sqrt{3}$ and $\sqrt{4}$ and again the lattice parameter was found to be 75 ± 1 Å. Electrodeposition from such a shear aligned H_1 phase was then carried out and the H_1-ePt film was prepared for SAXS analysis. Fig. 5a shows the corresponding 2D SAXS pattern; a clear set of spots was observed confirming that the film exhibited both short and long range order. Fig. 5b shows an azimuthal integration scan of the SAXS pattern for the film; as expected two peaks at 92 and 272° were observed, supporting in plane alignment of the nanostructure with respect to the electrode surface. FWHM values for the azimuthal peaks were found to be small, 10 ± 1 and 12 ± 1° respectively, suggesting that the nanostructure of the film was highly aligned and long

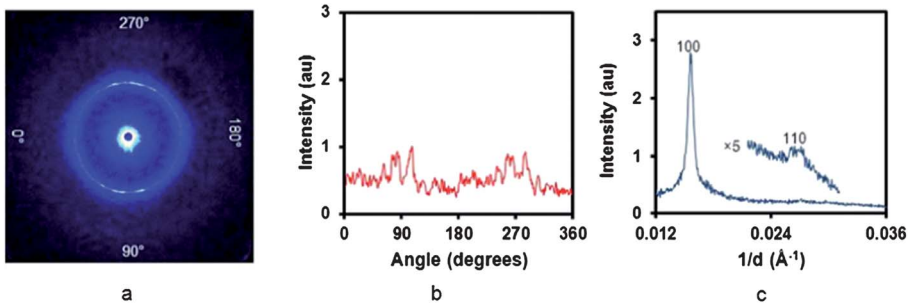

Fig. 2 SAXS analysis of an electrodeposited multi domain H_1-ePt film (Q = 0.54 C cm^{-2}); (a) 2D-SAXS pattern collected over 1800 s, (b) azimuthally integrated 1D SAXS pattern (inner ring) and (c) radially integrated 1D SAXS pattern.

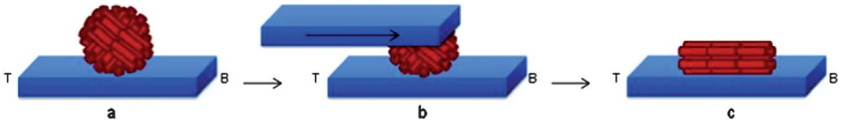

Fig. 3 A schematic diagram to show the method of shear alignment of a hexagonal (H_1) templating phase. (a) Represents an unaligned phase, (b) represents a phase under shear and (c) represents an aligned phase produced by the application of a shear force. The symbols 'T' and 'B' refer to the top and the bottom of the electrode respectively.

ranging. Fig. 5c shows the corresponding radial integration scan; two Bragg peaks typical of hexagonal symmetry with relative peak positions of $\sqrt{1} : \sqrt{3}$, were observed confirming the presence of the expected short range order in the film. The lattice parameter for this film was found to be 77 ± 1 Å which again is in good agreement with the templating phase itself.

It was noted that the underlying electrode exhibited a ridged surface (Fig. SI1a†) and experiments with the shear direction first parallel and second perpendicular, to the ridges showed that in each case, in plane alignment of the nanostructure parallel to the direction of shear was obtained. Data to support this are shown in ESI (Fig. SI5 and SI6†).

To investigate the control of pore orientation further the two types of H_1-ePt film [(i) unaligned (exhibiting short range pore order only) and (ii) aligned (exhibiting both short and long range pore order)] were subject to a grazing-incidence SAXS (GI-SAXS) study. The value of carrying out this study was that GI-SAXS, unlike transmission SAXS, has the ability to distinguish between uniaxial and biaxial pore alignment.

In the first instance GI-SAXS was performed with the beam passing parallel to the direction of shear, that is from the top (T) to the bottom (B) of the electrode [a schematic diagram showing sample loading is given in the ESI (Fig. SI7†)]. The GI-SAXS results are shown in Fig. 6. Fig. 6a presents 2D data for an unaligned H_1-ePt film; a scattering ring corresponding to the first Bragg peak for the hexagonal symmetry was observed. These data coupled with the transmission SAXS data confirm that the hexagonal pore structure is multi domain, with domains distributed randomly in 3D space. Fig. 6b presents 2D data for an aligned H_1-ePt film; a clear spot pattern was observed with the positions corresponding to the Bragg reflections for hexagonal symmetry.[44] The GI-SAXS pattern shows the {100}, {110} and {200} sets of reflections consistent with pores oriented parallel to the X-ray beam and therefore to the direction of shear; a schematic representation is shown in Fig. 6c where a {100} and a {200} vector are perpendicular to the substrate, and a {110} vector is parallel to it. These data confirm that in the aligned film the hexagonal pore structure is monodomain, the pores lie in plane with the support electrode, and they are biaxial with respect to the direction of shear. In other words, not only are the pores all aligned parallel to the direction of shear but the arrangement of the pores in the hexagonal array is such that the hexagons have a side rather than a corner pointing downwards as shown in Fig. 6c. This information is not accessible using transmission SAXS alone however these results do explain why, for such highly aligned samples, the transmission SAXS patterns (as in Fig. 5) can show relatively intense (110) reflections.

These results clearly show that shearing the templating phase results in the alignment of the phase at the surface of the electrode, as illustrated in Fig. 7a; subsequent electrodeposition produces a film where the hexagonal nanostructure also lies parallel to the substrate surface, with biaxial alignment, as depicted in Fig. 7b. Interestingly when the aligned hexagonal phase was subject to heat treatment (the temperature was increased from 30 to 70 °C followed by cooling back to 30 °C prior to electrodeposition) films with even greater alignment were produced, see ESI (Fig. SI8†).

Transmission electron microscopy (TEM) was also used to investigate the H_1-ePt film nanostructure, and representative images are shown in ESI (Fig. SI9†). The diameter of the pores was found to be 2.4 ± 0.2 nm. Whilst TEM images are a useful aid in terms of visualising the nanostructure, it must be remembered that the sample has to be removed from the underlying electrode in order to perform this kind of analysis and hence no information regarding the orientation of the pore structure with respect to the underlying electrode surface can be obtained. In addition TEM, being high resolution, only allows small portions of the film to be observed at any one time. In contrast both transmission SAXS and GI-SAXS can be performed on mesoporous films *in situ* (still attached to the underlying electrode)

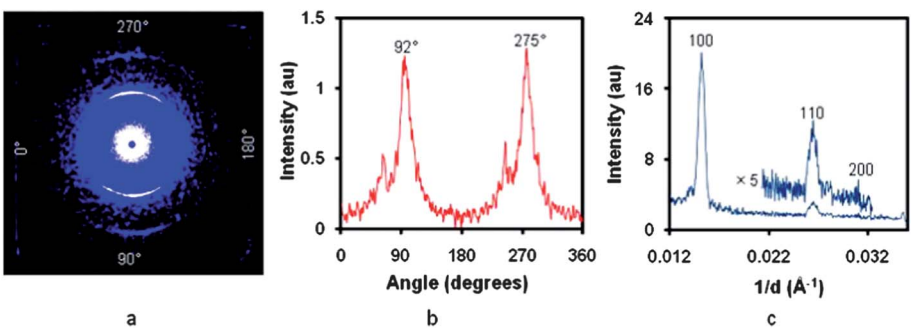

Fig. 4 SAXS analysis of a shear aligned $C_{16}EO_{10}$–H_2O hexagonal (H_1) phase; (a) 2D SAXS pattern collected over 600 s, (b) azimuthally integrated 1D SAXS pattern (inner ring) and (c) radially integrated 1D SAXS pattern (inset shows a magnified portion), all collected at 30 °C.

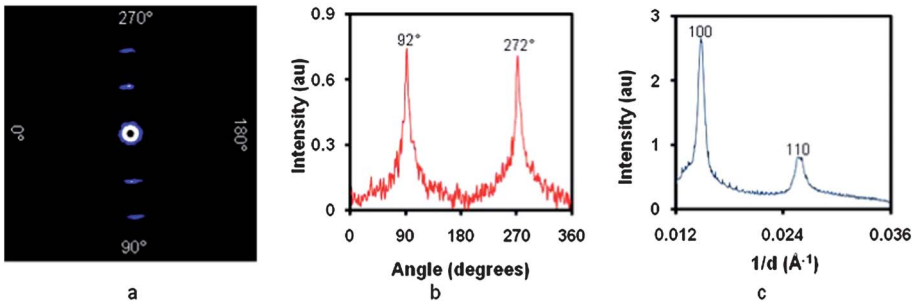

Fig. 5 SAXS analysis of a H_1-ePt film electrodeposited from a shear aligned phase ($Q = 0.54$ C cm^{-2}); (a) 2D-SAXS pattern collected over 1800 s, (b) azimuthally integrated 1D SAXS pattern (inner ring) and (c) radially integrated 1D SAXS pattern.

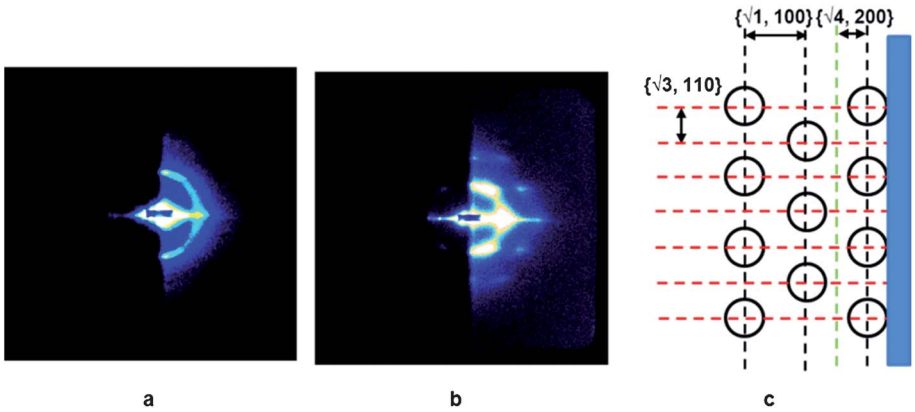

Fig. 6 2D GI-SAXS patterns of (a) a multi domain H_1-ePt film and (b) a H_1-ePt film electrodeposited from a shear aligned templating phase collected over 900 s respectively. Note the direction of the X-ray beam was parallel to the direction of shear as shown in ESI (Fig. SI7†); (c) A schematic representation of the aligned H_1-ePt films showing the pore orientation, and the corresponding SAXS reflections √1 {100}, √3 {110} and √4 {200}.

and the sample area is also larger. When used together these techniques can provide extensive information about nanostructure, short and long range order, pore alignment and pore orientation.

The two types of H_1-ePt film [(i) unaligned (exhibiting short range pore order only) and (ii) aligned (exhibiting both short and long range pore order)] were also subject to electrochemical analysis, using cyclic voltammetry in dilute sulfuric acid and in methanol. Fig. 8a and b show that in dilute sulfuric acid classic platinum in acid voltammograms were observed in both cases.[4,42] The currents passed at the mesoporous electrodes were very high (in comparison to the underlying support electrodes) and almost identical; analysis of the hydrogen under potential deposition region showed that the roughness factor (R_f) of the mesoporous

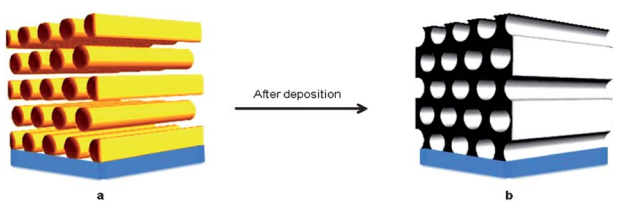

Fig. 7 A schematic representation of (a) the shear aligned H_1 templating phase and (b) the corresponding aligned H_1-ePt film produced by electrodeposition.

electrodes was similar (56 and 64 respectively) indicating that both types of pore structure were openly accessible to the electrolyte solution. Fig. 8c and d, show that similar behaviour was observed for methanol oxidation, indicating that pore alignment does not hinder the access of methanol to the mesoporous structure. The shape of the voltammograms were as expected[45] and the high currents observed show that both types of mesoporous structure were able to catalyse the oxidation of methanol well. It may be the case that subtle differences in behaviour exist and a more detailed investigation is certainly warranted given the great deal of interest that surrounds the electrochemical oxidation of methanol at nanostructured platinum surfaces.[45–50] Interestingly when one considers the case of an aligned biaxial pore structure, where the pores run parallel to the electrode surface, and one thinks about the aspect ratio of the pores, then one obtains a maximum theoretical value that is of the order of tens of thousands (2×10^5). This estimate is based on the following assumptions: the maximum pore length, 500 μm, is given by the diameter of the support electrode and the pore diameter, 2.4 nm, is given by TEM measurement. The pores however, may not be perfectly parallel with the electrode surface, and this coupled with the fact that the films are quite thin will reduce the pore length accordingly. Film thickness is estimated to be of the order of 165 nm; this is a reasonable estimate based on information gathered from cross-sectional SEM analysis (Fig. SI1c†) and information in the literature relating charge

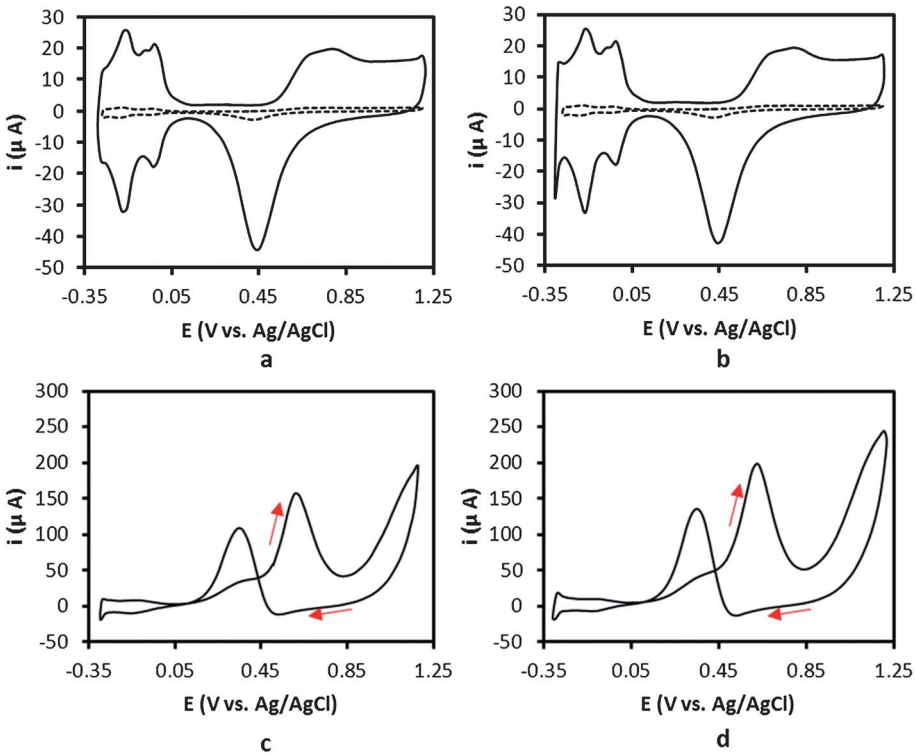

Fig. 8 Cyclic voltammograms recorded at 200 mV s^{-1} in 0.5 M H_2SO_4 and in 0.5 M H_2SO_4 plus 0.5 M CH_3OH for a H_1-ePt film ($Q = 0.5$ C cm^{-2}, $R_f = 56$) electrodeposited from a multi domain phase (a) and (c), and for a H_1-ePt film ($Q = 0.56$ C cm^{-2}, $R_f = 64$) electrodeposited from a shear aligned phase (b) and (d). Data for the polished platinum support electrodes (dotted lines) is also shown for comparison.

density to film thickness for a similar templating system.[42] To gain a better understanding of the actual pore length, the angle between the substrate and the pores was investigated using GI-SAXS analysis. This time the experiment was set up with the sample loaded vertically, with the beam passing perpendicular to the direction of shear [a schematic diagram showing sample loading is given in the ESI (Fig. SI10†)]. The corresponding 2D SAXS pattern and 1D azimuthally integrated plot are shown in ESI (Fig. SI11†). The azimuthal plot shows a sharp peak, the peak is centered at 179° and has a FWHM value of 2.5 ± 0.5° suggesting excellent uniformity of the structure, where the pores are at an angle, Ø, of 1–3° with respect to the electrode surface. Taking the film thickness, and dividing through by sin Ø, a more typical, yet still high, aspect ratio of ~2500 is obtained.

These results clearly show that the physical interaction of the templating phase with the electrode surface prior to electrodeposition is of great importance and can significantly affect the long range structure of a H_1-ePt film. This paper represents the first detailed study of this phenomena and is thus of widespread interest.

Conclusions

The orientation and the degree of alignment of the H_1 phase of an inexpensive and commercially available surfactant $C_{16}EO_{10}$ can be controlled using shear force. Importantly electrodeposition of platinum metal from a shear aligned templating phase transfers the short and long range order of the phase to the deposited material yielding nanostructured H_1-ePt films with a high degree of structural order, biaxial in plane pore alignment, and a lattice parameter similar to that of the H_1 phase (~75 Å). The pore structure has a high aspect ratio, and hence high surface area, and although lying parallel to the electrode surface, it remains accessible to electrolyte solution. This method of producing highly aligned, 2D mesoporous films, containing high aspect ratio biaxial pores, is simple and can potentially be used to produce a range of other materials with similar structures.

Acknowledgements

We thank the Department of Chemistry, University of Engineering and Technology Lahore-54890, Pakistan and the University of Reading for providing funding for KA. We thank the University of Reading Chemical Analysis Facility (CAF) and the Centre for Advanced Microscopy for providing access to instrumentation. We would also like to thank Dr Martyn Rittman, University of Reading, for providing assistance with the GI-SAXS analyses and the structure simulation.

References

1 C. T. Kresge, M. E. Leonowicz, W. J. Roth, J. C. Vartuli and J. S. Beck, *Nature*, 1992, **359**, 710–712.
2 G. S. Attard, J. C. Glyde and C. G. Goltner, *Nature*, 1995, **378**, 366–368.
3 G. S. Attard, J. M. Corker, C. G. Göltner, S. Henke and R. H. Templer, *Angew. Chem., Int. Ed. Engl.*, 1997, **36**, 1315–1317.
4 G. S. Attard, P. N. Bartlett, N. R. B. Coleman, J. M. Elliott, J. R. Owen and J. H. Wang, *Science*, 1997, **278**, 838–840.
5 I. W. Hamley, *Angew. Chem., Int. Ed.*, 2003, **42**, 1692–1712.

6 Y. Yamauchi, N. Suzuki, L. Radhakrishnan and L. Wang, *Chem. Rec.*, 2010, **9**, 321–339.
7 A. Chen and P. Holt-Hindle, *Chem. Rev.*, 2010, **110**, 3767–3804.
8 G. S. Attard, N. R. B. Coleman and J. M. Elliott, in *Studies in Surface Science and Catalysis*, Elsevier, 1998, vol. 117, pp. 89–94.
9 P. N. Bartlett, B. Gollas, S. Guerin and J. Marwan, *Phys. Chem. Chem. Phys.*, 2002, **4**, 3835–3842.
10 S. Li, M. S. Toprak, H. M. A. Soliman, J. Zhou, M. Muhammed, D. Platzek and E. Mueller, *Chem. Mater.*, 2006, **18**, 3627–3633.
11 J. Guo, H. Wu, F. Chen, L. Zhang, W. He, H. Yang and J. Wei, *J. Mater. Chem.*, 2010, **20**, 4094–4102.
12 P. V. Braun, P. Osenar and S. I. Stupp, *Nature*, 1996, **380**, 325–328.
13 I. Nandhakumar, J. M. Elliott and G. S. Attard, *Chem. Mater.*, 2001, **13**, 3840–3842.
14 P. A. Nelson, J. M. Elliott, G. S. Attard and J. R. Owen, *J. New Mater. Electrochem. Syst.*, 2002, **5**, 63–65.
15 J. M. Elliott, P. R. Birkin, P. N. Bartlett and G. S. Attard, *Langmuir*, 1999, **15**, 7411–7415.
16 P. N. Bartlett, P. N. Birkin, M. A. Ghanem, P. de Groot and M. Sawicki, *J. Electrochem. Soc.*, 2001, **148**, C119–C123.
17 A. H. Whitehead, J. M. Elliott, J. R. Owen and G. S. Attard, *Chem. Commun.*, 1999, 331–332.
18 D. H. Pamela, J. Hagrman and J. Zubieta, *Angew. Chem., Int. Ed.*, 1999, **38**, 2638–2684.
19 G. S. Attard, S. A. A. Leclerc, S. Maniguet, A. E. Russell, I. Nandhakumar and P. N. Bartlett, *Chem. Mater.*, 2001, **13**, 1444.
20 J. H. Ding and D. L. Gin, *Chem. Mater.*, 1999, **12**, 22–24.
21 S. Baber, M. Zhou, Q. L. Lin, M. Naalla, Q. X. Jia, Y. Lu and H. M. Luo, *Nanotechnology*, 2010, **21**, 1–9.
22 M. E. Davis, *Nature*, 2002, **417**, 813–821.
23 M. Y. Nie and J. M. Elliott, *J. Mater. Sci. Technol.*, 2005, **21**, 863–865.
24 J. Kuleshova, P. R. Birkin and J. M. Elliott, *J. Phys. Chem. C*, 2010, **114**, 13442–13450.
25 P. R. Birkin, J. M. Elliott and Y. E. Watson, *Chem. Commun.*, 2000, 1693–1694.
26 J. Kuleshova, P. R. Birkin and J. M. Elliott, *J. Electroanal. Chem.*, 2009, **636**, 68–73.
27 S. A. G. Evans, J. M. Elliott, L. M. Andrews, P. N. Bartlett, P. J. Doyle and G. Denuault, *Anal. Chem.*, 2002, **74**, 1322–1326.
28 T. Imokawa, K.-J. Williams and G. Denuault, *Anal. Chem.*, 2006, **78**, 265–271.
29 P. Lozano-Sanchez and J. M. Elliott, *Analyst*, 2008, **133**, 256–262.
30 A. Yamaguchi, F. Uejo, T. Yoda, T. Uchida, Y. Tanamura, T. Yamashita and N. Teramae, *Nat. Mater.*, 2004, **3**, 337–341.
31 Q. Fu, G. V. Rama Rao, T. L. Ward, Y. Lu and G. P. Lopez, *Langmuir*, 2007, **23**, 170–174.
32 J. S. Biggins, M. Warner and K. Bhattacharya, *Phys. Rev. Lett.*, 2010, **103**, 1–4.
33 H. Miyata, Y. Fukushima, K. Okamoto, M. Takahashi, M. Watanabe, W. Kubo, A. Komoto, S. Kitamura, Y. Kanno and K. Kuroda, *J. Am. Chem. Soc.*, 2011, **133**, 13539–13544.
34 M. Hartmann, *Chem. Mater.*, 2005, **17**, 4577–4593.
35 C. J. Brinker and D. R. Dunphy, *Curr. Opin. Colloid Interface Sci.*, 2006, **11**, 126–132.
36 K. C. W. Wu, X. Jiang and Y. Yamauchi, *J. Mater. Chem.*, 2011, **21**, 8934–8939.
37 E. L. Crepaldi, G. Soler-Illia, D. Grosso, F. Cagnol, F. Ribot and C. Sanchez, *J. Am. Chem. Soc.*, 2003, **125**, 9770–9786.
38 L. Radhakrishnan, H. Wang and Y. Yamauchi, *Chem.–Asian J.*, 2010, **5**, 1290–1293.
39 T. Brezesinski, M. Antonietti and B. M. Smarsly, *Adv. Mater.*, 2007, **19**, 1074–1078.
40 G. S. Attard, P. N. Bartlett, N. R. B. Coleman, J. M. Elliott and J. R. Owen, *Langmuir*, 1998, **14**, 7340–7342.
41 S. L. Gras and A. M. Squires, in *Protein Folding, Misfolding, and Disease: Methods and Protocols*, ed. A. F. Hill, K. J. Barnham, S. P. Bottomley and R. Cappai, 2011, vol. 752, pp. 147–163.
42 J. M. Elliott, G. S. Attard, P. N. Bartlett, N. R. B. Coleman, D. A. S. Merckel and J. R. Owen, *Chem. Mater.*, 1999, **11**, 3602–3609.
43 J. M. Seddon and R. H. Templer, in *Handbook of Biological Physics*, ed. R. Lipowsky and E. Sackmann, North-Holland, 1995, vol. 1, pp. 97–160.
44 D. Pan, W. C. Wang, W. H. Liu, L. Yang and H. W. Huang, *J. Am. Chem. Soc.*, 2006, **128**, 3800–3807.
45 J. M. Elliott, G. S. Attard, P. N. Bartlett, J. R. Owen, N. Ryan and G. Singh, *J. New Mater. Electrochem. Syst.*, 1999, **2**, 239–241.
46 A. Kucernak and J. Jiang, *Chem. Eng. J.*, 2003, **93**, 81–90.
47 E. P. Lee, Z. Peng, W. Chen, S. Chen, H. Yang and Y. Xia, *ACS Nano*, 2008, **2**, 2167–2173.
48 L. Liu, E. Pippel, R. Scholz and U. Goesele, *Nano Lett.*, 2009, **9**, 4352–4358.
49 M. Rauber, I. Alber, S. Mueller, R. Neumann, O. Picht, C. Roth, A. Schoekel, M. E. Toimil-Molares and W. Ensinger, *Nano Lett.*, 2011, **11**, 2304–2310.
50 K. S. Choi, E. W. McFarland and G. D. Stucky, *Adv. Mater.*, 2003, **15**, 2018–2021.